nature materials

Article

https://doi.org/10.1038/s41563-023-01580-7

Intrinsic strong light-matter coupling with self-hybridized bound states in the continuum in van der Waals metasurfaces

Received: 31 August 2022

Accepted: 17 May 2023

Published online: 22 June 2023

Check for updates

Thomas Weber[1], Lucca Kühner[1], Luca Sortino[1], Amine Ben Mhenni[2], Nathan P. Wilson[2], Julius Kühne[1], Jonathan J. Finley[2], Stefan A. Maier[1,3,4] & Andreas Tittl[1]

Photonic bound states in the continuum (BICs) provide a standout platform for strong light-matter coupling with transition metal dichalcogenides (TMDCs) but have so far mostly been implemented as traditional all-dielectric metasurfaces with adjacent TMDC layers, incurring limitations related to strain, mode overlap and material integration. Here, we demonstrate intrinsic strong coupling in BIC-driven metasurfaces composed of nanostructured bulk tungsten disulfide (WS_2) and exhibiting resonances with sharp, tailored linewidths and selective enhancement of light-matter interactions. Tuning of the BIC resonances across the exciton resonance in bulk WS_2 is achieved by varying the metasurface unit cells, enabling strong coupling with an anticrossing pattern and a Rabi splitting of 116 meV. Crucially, the coupling strength itself can be controlled and is shown to be independent of material-intrinsic losses. Our self-hybridized metasurface platform can readily incorporate other TMDCs or excitonic materials to deliver fundamental insights and practical device concepts for polaritonic applications.

Understanding and maximizing the interaction between light and matter in nanoscale materials is a central goal of nanophotonics. Resonant nanosystems have been investigated for the confinement and control of electromagnetic energy in sub-wavelength volumes, leading to breakthroughs in light harvesting[1], optical waveguiding[2] and emission control[3]. Coupling light to electronic excitations in solid-state materials is of particular interest because of the creation of hybridized photonic and electronic states, called polaritons, showing exciting properties such as Bose–Einstein condensation[4] and superfluidity[5] with potential for applications in low-threshold semiconductor lasers[6], photocatalytic enhancement[7] and quantum computing[8]. The driving force for research on excitonic coupling has been reaching the strong light-matter coupling regime, where coherent exchange of energy between photons and excitons takes place. Transition metal dichalcogenides (TMDCs) are a promising class of van der Waals materials for strong light-matter coupling, as they host strongly bounded excitons that are stable up to room temperature, owing to large binding energies >200 meV (ref. 9), coupled valley and spin degrees of freedom and broad tunability through strain, dielectric environment and the DC Stark effect[10–12]. TMDCs exhibit large excitonic oscillator strengths even in ~10–100 nm thick films[13], rendering this class of materials compatible with established architectures of flat-optics devices to study strong light-matter interaction.

In general, reaching the strong coupling regime in nanophotonic systems requires high electromagnetic field intensities, confinement of light into small modal volumes and maximum overlap between the optical modes of the cavity and the excitonic resonances in the material. To date, strong coupling has been realized with TMDC monolayers in

[1]Chair in Hybrid Nanosystems, Nanoinstitute Munich, Faculty of Physics, Ludwig-Maximilians-Universität München, Munich, Germany. [2]Walter Schottky Institut, Department of Physics, School of Natural Sciences, Technische Universität München, Garching, Germany. [3]School of Physics and Astronomy, Monash University, Clayton, Victoria, Australia. [4]Department of Physics, Imperial College London, London, UK. e-mail: andreas.tittl@physik.uni-muenchen.de

a variety of photonic systems, including plasmonic nanoantennas[14,15], photonic crystals[16,17] and distributed Bragg reflector microcavities[18], as well as in self-hybridizing structures such as bulk TMDC slabs acting as Fabry–Perot cavity[19] and single nanostructures supporting Mie resonances[20].

Recently, photonic bound states in the continuum (BICs) have been shown to provide excellent control over light-matter interactions, owing to their strongly enhanced near fields, high quality factors and broad resonance tunability via variation of their geometrical parameters. Consequently, BICs have established themselves as essential new building blocks for nanophotonic vibrational spectroscopy[21,22], light guiding[23], harmonic generation[24] and lasing[25]. Symmetry-protected metasurfaces[26] have emerged as a prominent platform to realize BIC resonances for light-matter coupling applications, owing to their high optical signal contrasts even when subjected to fabrication imperfections[27], and ease of optical measurements requiring only common brightfield microscopy setups. Importantly, the BIC metasurface concept provides direct control over the radiative decay rate (and therefore the linewidth) of the resonances via the asymmetry of the constituent unit cells[26].

Currently, many implementations of excitonic strong coupling with BICs rely on placing TMDC layers adjacent to BIC metasurfaces composed of traditional all-dielectric materials such as Si, TiO_2, Si_3N_4 or Ta_2O_5 (refs. 17,28–31). However, this approach increases system complexity due to the direct contact between different material systems and inhomogeneities introduced during the TMDC transfer process, where topographic irregularities and strain in the TMDC layers can lead to spectral shifts of the exciton[32] or the suppression of non-linear effects[33]. Additionally, light-matter interaction occurs only via the evanescent fields around the BIC resonators, which decreases the coupling strength, especially when incorporating commonly used buffer layers for TMDCs, such as hexagonal boron nitride. Obtaining a TMDC BIC platform, which combines photonic cavity and excitonic material in the same nanostructured system, is therefore highly desirable; however, an experimental demonstration is still lacking.

Here, we realize precisely controlled strong coupling in self-hybridized WS_2 metasurfaces based on symmetry-protected BICs. The metasurface platform consists of arrays of rod-type BIC unit cells, where the asymmetry of the structure is controlled via the length difference ΔL of the rods, offering direct control over the resonance linewidth. We experimentally demonstrate strong coupling with pronounced and tunable BIC resonances in WS_2 metasurfaces fabricated via mechanical exfoliation, electron-beam lithography (EBL) and reactive-ion etching (RIE) (see Methods for more details). Resonance quality factors approach $Q = 370$ at spectral positions close to but spectrally separated from the exciton.

By varying the lateral size of the metasurface unit cells, the BIC resonances are tuned across the WS_2 exciton, which reveals an anticrossing pattern with a Rabi splitting of 116 meV at ambient conditions, which is three times larger than the linewidths of the underlying excitonic and photonic resonances, propelling the system well into the strong coupling regime. Using the versatile resonance control afforded by the BIC concept, our experiments reveal a clear increase of the Rabi splitting with lower asymmetries, which we attribute to a complex interplay between radiative quality factor and mode volume.

In sharp contrast to previous intrinsic coupling approaches based on anapoles[20] or wires[34], our results incorporate precise control of the radiative loss channel to achieve tunable coupling strengths and polariton populations.

Numerical metasurface design

WS_2 was chosen for our BIC metasurface realization because of its spectrally isolated exciton at 629 nm for the bulk material, its large oscillator strength compared with other TMDCs such as MoS_2, $MoSe_2$ or WSe_2 (ref. 13) and its high refractive index ($n = 4.1$ at $\lambda = 800$ nm). Our design adopts a rod-type BIC unit cell geometry (Fig. 1a) with precise control over the asymmetry via the length difference ΔL_0, spectral tunability via a multiplicative scaling factor S, high signal modulation and a spectrally clean mode structure. The WS_2 metasurfaces were numerically optimized to simultaneously obtain spectral overlap of the BIC resonances with the exciton, strong near-field enhancements and compatibility with nanofabrication tolerances. To capture the optical response of the WS_2 BIC metasurface with and without the influence of the exciton, we modelled the refractive index of WS_2 as a Tauc–Lorentz dielectric (Fig. 1b and Methods). We demonstrated the existence of a BIC on the low-energy side of the exciton with full-wave simulations and showed the capability to spectrally tune the BIC via the geometric scaling factor S (Fig. 1c), and to control the resonance linewidth with a varying asymmetry parameter ΔL_0 (Fig. 1d). At resonance, the electric near field εE, where ε is the permittivity of WS_2 or air, is concentrated inside the structure (Fig. 1e), leading to an enhancement of the light-matter interaction. To analyse the loss channels associated with the BIC modes, we employed a temporal coupled mode theory model to fit the simulated transmittance spectra. This approach allowed us to decompose the quality factors of the BICs into their radiative and intrinsic parts, where the radiative contribution shows the expected characteristic inverse square law with asymmetry. The intrinsic part incorporates all non-radiative loss channels such as material absorption, surface roughness or edge losses[35] and is described by our effective material parameters (Methods). Due to small losses in the material, the total Q factor is limited by the intrinsic quality factor, which leads to a deviation of the inverse square dependence. Additionally, the BIC-driven light-matter interaction is governed by critical coupling[36], where the highest field enhancement is achieved when the radiative and intrinsic Q factors match (Fig. 1e,f).

Metasurface fabrication and optical characterization

The fabrication process began with mechanical exfoliation of bulk WS_2 flakes onto fused silica substrates (Fig. 2a), with flake thicknesses ranging from 30 to 50 nm. The exfoliated WS_2 flakes were then patterned via EBL and RIE (Methods). Scanning electron microscope micrographs for different asymmetry parameters revealed the accurate reproduction of the metasurface design with high uniformity and surface quality (Fig. 2b). The transmittance spectra of the fabricated structures were measured in an optical spectroscopy setup. We illustrated the emergence of the BIC mode from the symmetric case by gradually increasing the asymmetry parameter ΔL_0. The corresponding transmittance spectra (Fig. 2c) clearly show a spectral blueshift and linewidth broadening with increasing asymmetry and the extracted Q factors range from 20 to 370, with highest values found for the lowest asymmetries (Fig. 2d).

As already seen in the simulations, the total Q factor is limited by the material-intrinsic absorption as well as scattering losses due to surface roughness and statistical variations[27]. Overall, we see excellent agreement between experimental and simulated results, although the radiative Q factor slightly deviates from the characteristic inverse square dependence of the BIC due to small uncertainties in the fits of the experimental spectra for low asymmetries caused by small signal modulations.

BIC-driven intrinsic strong coupling

To demonstrate metasurface-based strong light-matter coupling, we tuned the BIC resonances over the WS_2 exciton wavelength at 629 nm (1.971 eV). The spectral tuning was achieved by fabricating 11 metasurface patches with an asymmetry parameter of $\Delta L_0 = 80$ nm with scaling factors between $S = 0.9$ and $S = 1.2$ from a single WS_2 flake with a height of $h = 45$ nm. Transmittance spectra of the metasurface patches show clear anticrossing behaviour, which is a necessary feature of the strong coupling regime (Fig. 3a). The full energy dispersion of the system is shown in Fig. 3b and is plotted against energy to facilitate the

https://doi.org/10.1038/s41563-023-01580-7

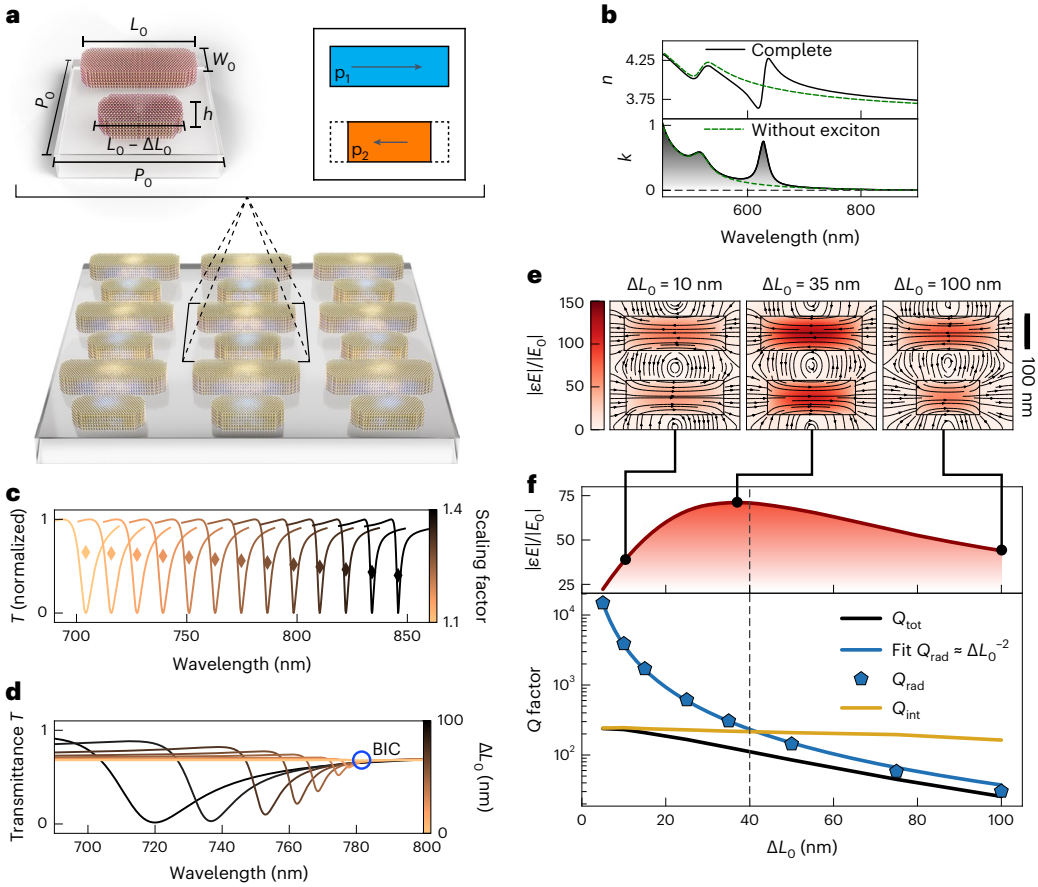

Fig. 1 | Bound states in the continuum in bulk WS_2 metasurfaces. a, Rod-type symmetry-protected BIC unit cell showing the working principle of opposing electric dipoles (denoted by p_1 and p_2). The geometrical unit cell parameters are fixed as: periodicity $P_0 = 340$ nm, base rod length $L_0 = 266$ nm and rod width $W_0 = 90$ nm. The centre points of the rods are placed at the unit cell coordinates $(x, y) = (0, P/4)$ and $(0, 3P/4)$. Tunability of the resonance position is realized by introducing a multiplicative scaling factor S, which scales the in-plane geometrical parameters according to $P = SP_0$, $L = SL_0$, $\Delta L = S\Delta L_0$ and $W = SW_0$. h, height. **b**, Tauc–Lorentz material of WS_2 showing the real part n and imaginary part k of the in-plane complex refractive index with and without the exciton. **c**, Simulated transmittance spectra of BIC resonances on the low-energy side of the exciton tuned via scaling of the in-plane geometric parameters. The markers indicate the modulation of the transmittance signal. **d**, Simulated transmittance spectra of BICs for different asymmetries ΔL_0. Smaller asymmetries lead to a spectral redshift and a reduction of the linewidth. For symmetric structures the resonance vanishes as the quasi-BIC turns into a true BIC. **e**,**f**, Electric field enhancements and quality factors for different asymmetry parameters ΔL_0. The maximum field enhancement is achieved when both intrinsic and radiative damping rates of the BIC mode are matched (**e**). The radiative quality factor follows the expected inverse square dependence of a BIC. The intrinsic Q factor shows a slight increase for lower asymmetries due to a slightly larger extinction value of the blue-shifted BIC (**f**). The total Q factor follows the radiative Q factor for large asymmetries and is dominated by the intrinsic Q factor for small asymmetries.

subsequent analysis. The energies of the upper and lower polariton branches can be calculated from

$$\omega_{\pm} = \frac{\omega_{BIC}+\omega_{Ex}}{2} + \frac{i(\gamma_{BIC}+\gamma_{Ex})}{2} \pm \sqrt{g^2 - \frac{1}{4}(\gamma_{BIC} - \gamma_{Ex} + i(\omega_{BIC} - \omega_{Ex}))^2}, \quad (1)$$

where ω_{Ex} and γ_{Ex} indicate the frequency and the exciton damping rate, ω_{BIC} and γ_{BIC} are the resonance frequency and damping rate of the BIC, respectively, g is the coupling strength between the two coupled systems and i is the imaginary unit (Supplementary Note 2). The corresponding Rabi splitting is defined as $\Omega_R = 2\sqrt{g^2 - (\gamma_{BIC} - \gamma_{Ex})^2/4}$. The properties of the exciton are extracted from transmission measurements on a symmetric metasurface patch without the presence of a BIC mode, yielding $\hbar\omega_{Ex} = 1.971$ eV and $\hbar\gamma_{Ex} = 36$ meV. The linewidth of the BIC at the wavelength of the exciton is obtained from simulations as $\hbar\gamma_{BIC} = 30$ meV (Fig. 3c). We can now fit equation (1) to the experimentally obtained energies of the polariton branches to obtain a Rabi splitting of (116 ± 4) meV. Two established criteria of strong coupling[30,37]

$$c_1 = \Omega_R/(\gamma_{BIC} + \gamma_{Ex}) > 1 \quad (2)$$

$$c_2 = g/\sqrt{(\gamma_{BIC}{}^2 + \gamma_{Ex}{}^2)/2} > 1 \quad (3)$$

yield $c_1 = 1.75$ and $c_2 = 1.74$, respectively, exceeding the required conditions substantially and verifying that our BIC-driven metasurface concept indeed reaches the strong coupling regime. These findings are further supported by analysing the influence of potential uncertainties in our fitting scheme (Supplementary Fig. 5).

Furthermore, we investigated the influence of temperature on the coupling process by measuring the transmittance spectra of the WS_2 BIC metasurface at different temperatures in a cryostat. The optical performance of the metasurface is maintained even at cryogenic temperatures, and comparing the experiments at room temperature and 5 K, the expected spectral blueshift of the exciton[38] is visible (Supplementary Fig. 7a). Although the Rabi splitting shows a small declining trend with decreasing temperatures (Supplementary Fig. 7b), which we ascribe to the reduction of the oscillator strength for the phonon-mediated

https://doi.org/10.1038/s41563-023-01580-7

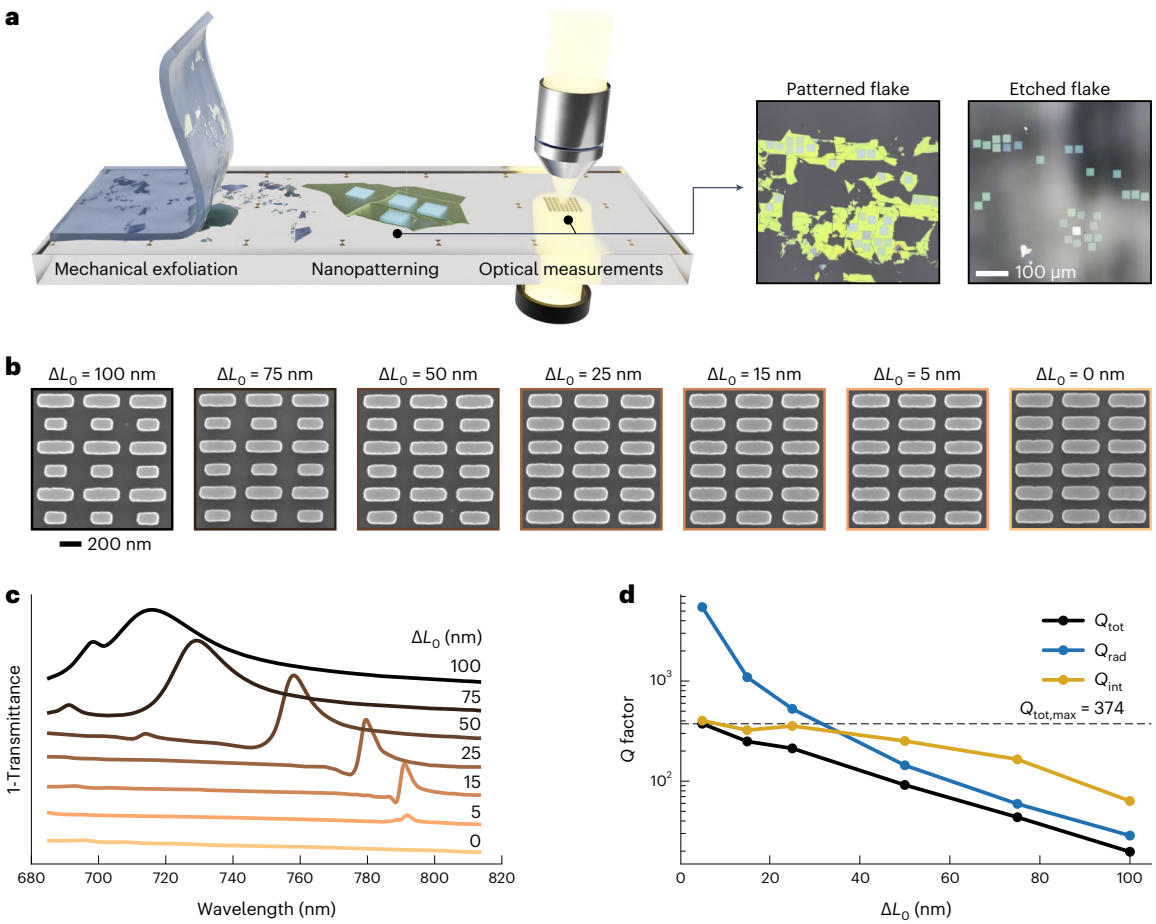

Fig. 2 | Experimental realization of bulk WS_2 BIC metasurfaces. a, Sketch of the experimental process including exfoliation of WS_2, nanopatterning via EBL and RIE and optical far-field spectroscopy. **b**, Scanning electron microscope micrographs of fabricated WS_2 metasurfaces with a scaling factor of $S = 1.25$ with different asymmetry parameters ΔL_0 and a uniform thickness of 80 nm. **c**, Transmittance spectra of WS_2 metasurfaces (shifted for visiblility) for different ΔL_0, showing the formation of the quasi-BIC modes. To show the uncoupled BIC modes, resonances were placed spectrally separated from the WS_2 exciton. **d**, Resonance Q factors extracted from the spectra in panel **c** showing a maximum Q factor of 374.

momentum indirect transition of the bright exciton, strong coupling is maintained down to 5 K.

Tailored strong coupling

To correlate BIC quality factor and Rabi splitting, we simulated and fabricated metasurfaces with different asymmetry factors ΔL_0 with a height of 33 nm. For higher asymmetries, the BIC resonances exhibit higher modulation contrasts combined with broader linewidths (Fig. 4a,b). On the other hand, we observe increased values of the Rabi splitting for lower asymmetries (Fig. 4c). This unique and previously unavailable tuning behaviour provides a new mechanism for tailoring the Rabi splitting using simple structural modification, and can thus enable the design of metasurface geometries with optimal ratio of resonance modulation to Rabi splitting in the strong coupling regime (Supplementary Fig. 6). For the lowest asymmetry of $\Delta L_0 = 20$ nm, the BIC resonances are strongly damped by the intrinsic losses of WS_2, and we can no longer resolve a clear peak splitting (grey shaded area in Fig. 4c).

Furthermore, we plotted the Rabi splitting against the radiative Q factors of the BIC resonances without exciton from simulations and observed that both the Rabi splitting and the coupling constant g undergo a steep increase at low Q factors and saturate at higher Q factors (Fig. 4d). The observed trend is consistent with predictions from the literature, where the saturation of the Rabi splitting is attributed to the saturation of the electric field enhancement[39,40]. However, in comparison with idealized lossless dielectric BIC-driven metasurfaces, where the field enhancement scales with the square root of the Q factor (Supplementary Fig. 9i) and thus shows a saturating behaviour, the field enhancement of realistically modelled WS_2 BIC metasurfaces is governed by critical coupling, which is influenced by background losses in the material. At the spectral position of the exciton, maximum field enhancement is achieved for $\Delta L_0 = 110$ nm (Fig. 4c) and shows an upward trend, which contrasts strongly with the downward trend of the Rabi splitting, implying that the Rabi splitting is independent of the electric near-field enhancement. This is also supported by additional simulations with lossless and lossy materials, showing identical Rabi splitting (Supplementary Fig. 9c,f).

The observed independence from the field enhancement is consistent with the common definition for the coupling strength g[41]

$$g \approx \mu \cdot E \approx \sqrt{\frac{N}{V_{\mathrm{eff}}}}, \tag{4}$$

where μ is the collective dipole moment of the exciton, E the local electric field strength, N the number of excitons participating in the coupling process and V_{eff} the effective mode volume. We calculated the effective mode volume, which follows the decreasing trend of the geometric volume, when increasing the asymmetry (Supplementary Note 5 and Supplementary Fig. 11), which would imply an increase of coupling strength. However, due to the reduced volume, fewer excitons partake in the coupling process, which effectively counteracts the

https://doi.org/10.1038/s41563-023-01580-7

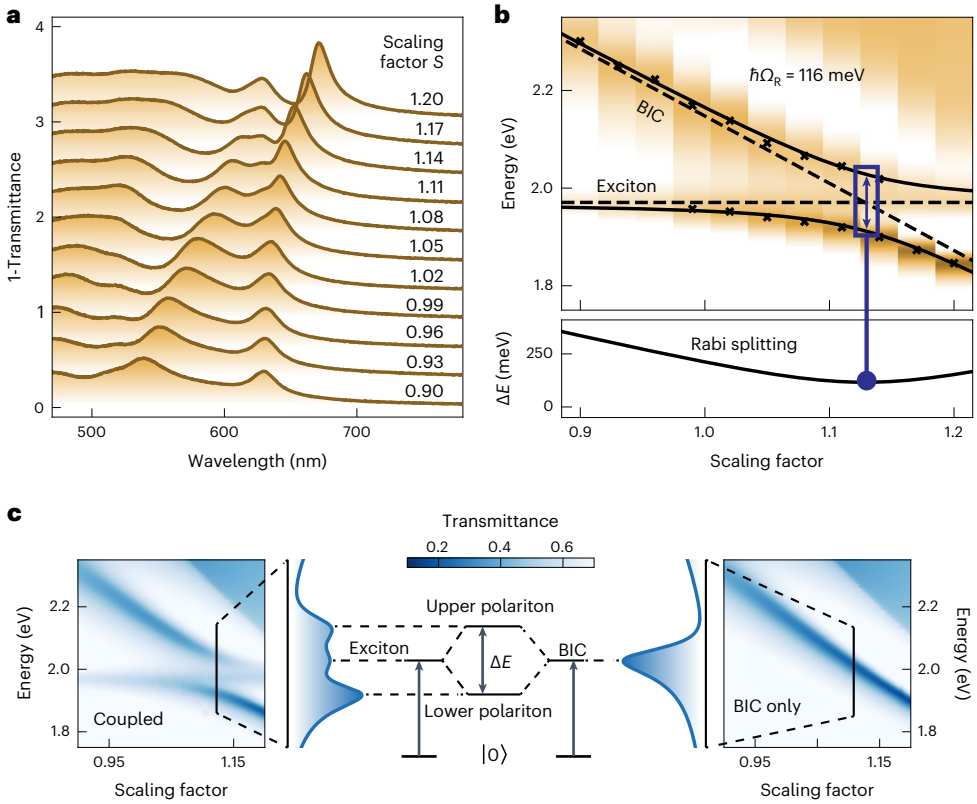

Fig. 3 | Strong coupling in WS_2 BIC metasurfaces. a, Experimental transmittance spectra of WS_2 BIC metasurfaces with an asymmetry parameter $\Delta L_0 = 80$ nm for different scaling factors show a characteristic anticrossing mode pattern close to the WS_2 exciton. **b**, The energy dispersion fit of both polariton branches reveals a Rabi splitting of 116 meV at room temperature. **c**, Simulations where the WS_2 BIC mode is continuously tuned over the spectral location of the WS_2 exciton by varying the scaling factor using dielectric functions from the Tauc–Lorentz model with and without the exciton. By aligning the spectral location of BIC and exciton, both modes hybridize into polaritonic branches with higher and lower energies compared with their uncoupled ground states.

effects of the reduction of mode volume, leading to constant exciton density and coupling strength. Notably, the above definition of the coupling strength is only valid for low-loss and non-radiative cavities[42]. A similar trend is observed for the optical confinement factor of the BIC structure (Supplementary Fig. 12).

Next, we separately studied the radiative and intrinsic loss channels that affect the total BIC Q factor. We used a simplified Lorentzian material representing a narrower exciton with a linewidth that is between the narrowest and the broadest BIC linewidths achievable with the given geometric parameters. When we change the Q factor by adding intrinsic losses to the system, we observe a constant coupling strength g and a Rabi splitting peaking at the maximum value $2g$ for matching linewidths of BIC and exciton (Supplementary Fig. 8a,b). The decrease of Rabi splitting for low Q factors is caused by the expected weakening of the strong coupling conditions towards the weak coupling regime (Supplementary Fig. 8c).

In contrast, when changing radiative losses through a variation of the asymmetry parameter ΔL_0, both the coupling strength and Rabi splitting follow the saturation trend described above, independent of intrinsic losses of the system, and the Rabi splitting reaches the value $2g$ when the linewidths of BIC and exciton match (Supplementary Fig. 9j). This shows that the general coupling rules are still valid, but that these effects are negligible compared with the overall trend. Importantly, the coupling strength itself is modified by varying the radiative Q factor, showing that our TMDC BIC platform is able to directly control the coupling conditions in the system.

Therefore, we deduced that the coupling strength (Supplementary Fig. 9c,f) is indeed independent of the electric near-field enhancement (Supplementary Fig. 9d,g). Moreover, considering the constant excitonic density, our analysis identified an additional mechanism for changing the coupling strength by controlling the radiative loss channel. While intrinsic losses change the Rabi splitting because of a linewidth broadening of the BIC, eventually turning to the weak coupling regime, energy is dissipated from the resonator system through the radiative loss channel to the far field, which reduces the interaction time of the photons with the excitons for large asymmetry parameters, thus lowering the coupling strength.

Even though the coupling strength itself is independent of any field-enhancing effect such as critical coupling, the population of the polariton branches is heavily influenced by it. When the radiative BIC quality factor is matched to both its intrinsic quality factor and the width of the exciton, the maximum absorbance for our system of 0.5 can be reached, which is known as strong critical coupling or polaritonic critical coupling[31] (Supplementary Fig. 10a–c). We numerically proved that this regime can be reached for our Tauc–Lorentz material with only small changes to the structure parameters of the BIC unit cell (Supplementary Fig. 10d).

Discussion

We have realized a self-hybridized WS_2 metasurface platform based on symmetry-protected BICs. We achieved resonances with total Q factors of up to 370 on the low-energy side of the exciton at wavelengths from 700 to 800 nm, demonstrating that exfoliated bulk TMDCs are an excellent material for all-dielectric nanophotonics owing to their high refractive index, low losses and mono-crystallinity. Moreover, we leveraged the precise control of the resonance position of the BIC mode via geometric variations to tune the BIC spectrally to the material-intrinsic excitonic resonance at 629 nm, leading to strong light-matter interaction and hybridization of photonic and excitonic

https://doi.org/10.1038/s41563-023-01580-7

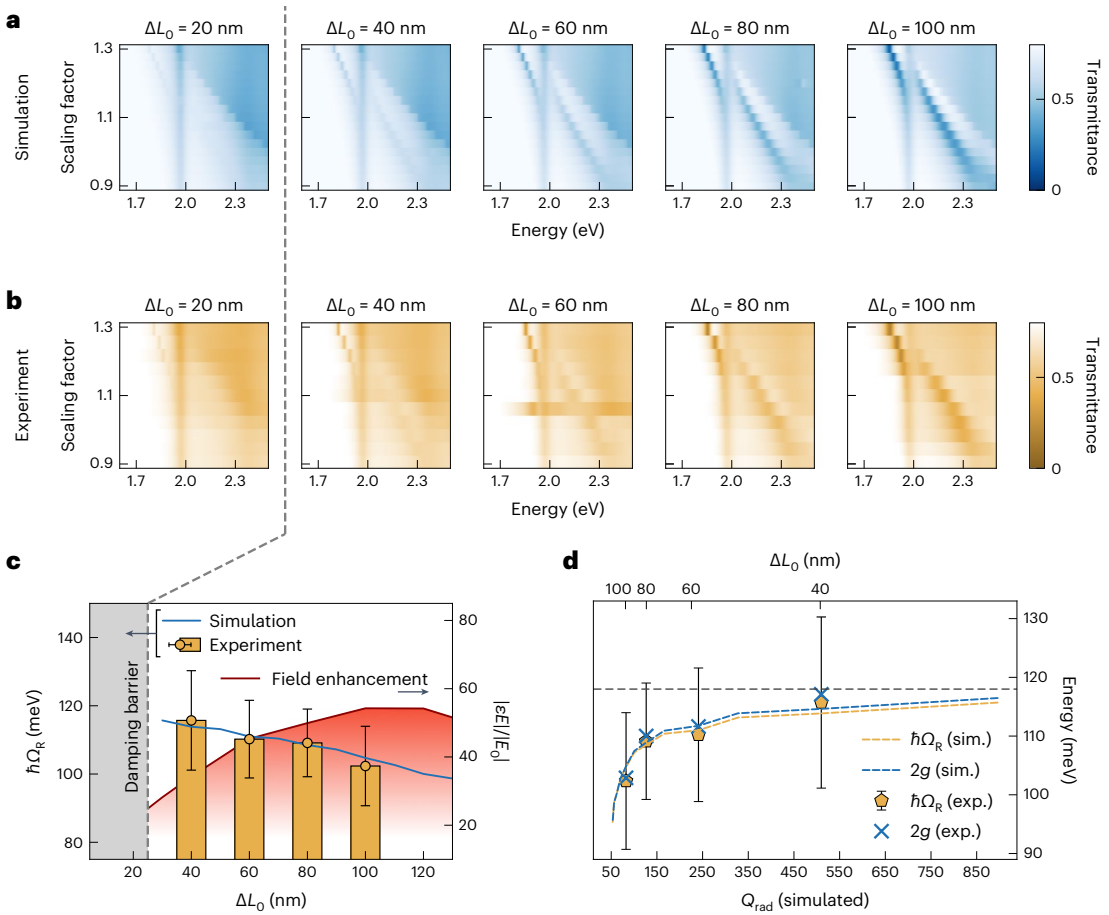

Fig. 4 | Tailored Rabi splitting in BIC metasurfaces. a,**b**, Simulated (**a**) and experimental (**b**) energy dispersion plots for WS_2 BIC metasurfaces for different asymmetry factors ΔL_0, enabling strong coupling experiments with multiple resonance quality factors and field confinements. **c**, Extracted Rabi splitting values from the data in **a** and averaged electric field enhancement in the resonator as a function of asymmetry parameter ΔL_0. The Rabi splitting decreases with increasing asymmetry, demonstrating the capability of tailouring light-matter coupling strength using photonic BICs. **d**, Rabi splitting values and coupling constants extracted from **b** as a function of the simulated radiative BIC quality factor saturating for high radiative quality factors. The error bars depict the standard error of the fit values. Exp., experimental; sim., simulated.

modes. We experimentally resolved a clear anticrossing pattern of the exciton-polariton branches with a Rabi splitting of 116 meV at temperatures ranging from 5 K to room temperature. By varying the radiative Q factor of the BIC via the asymmetry factor of the BIC unit cell between $\Delta L_0 = 40$ nm and $\Delta L_0 = 100$ nm, we were able to tune the Rabi splitting in a linear fashion, where the highest Rabi splitting value was reached for the largest Q factors. We have further shown that the Rabi splitting is independent of the electric near-field enhancement, rendering the coupling conditions of our TMDC BIC platform independent of the material-intrinsic losses. Furthermore, because of the precise control over the radiative coupling conditions of the BIC to the far field, we can tune the coupling strength directly, which is facilitated through a complex interplay between mode volume and temporal field confinement via the radiative loss channel.

In comparison with other strong coupling platforms such as anapole disks, bulk wires or hybrid plasmonic system, we achieved direct control over the coupling strength via tuning the radiative quality factor via the geometrical asymmetry factor. Moreover, our numerical simulations showed that we can maximize the population of the polariton branches by reaching the polaritonic critical coupling regime, which could be crucial for the development of efficient polaritonic devices.

Recent advances in the growth of high-quality bulk TMDC films via chemical vapour deposition[43] show a way forward to area-scalable TMDC BIC metasurfaces unrestricted by the size limitations of exfoliated crystals.

Through our generalized description of WS_2 as a Lorentz-type dielectric, our results are broadly applicable to other materials systems supporting resonant material-intrinsic responses such as perovskites or other van der Waals materials like black phosphorus and hexagonal boron nitride, which could pave the way for robust, tunable and efficient polaritonic devices in a large wavelength region.

Online content

Any methods, additional references, Nature Portfolio reporting summaries, source data, extended data, supplementary information, acknowledgements, peer review information; details of author contributions and competing interests; and statements of data and code availability are available at https://doi.org/10.1038/s41563-023-01580-7.

References

1. Bi, Y.-G. et al. Nanostructures induced light harvesting enhancement in organic photovoltaics. *Nanophotonics* **7**, 371–391 (2017).
2. Bogaerts, W. et al. Nanophotonic waveguides in silicon-on-insulator fabricated with CMOS technology. *J. Lightwave Technol.* **23**, 401–412 (2005).
3. Decker, M. & Staude, I. Resonant dielectric nanostructures: a low-loss platform for functional nanophotonics. *J. Optics* **18**, 103001 (2016).
4. Kasprzak, J. et al. Bose–Einstein condensation of exciton polaritons. *Nature* **443**, 409–414 (2006).
5. Lerario, G. et al. Room-temperature superfluidity in a polariton condensate. *Nat. Phys.* **13**, 837–841 (2017).

6. Deng, H., Weihs, G., Snoke, D., Bloch, J. & Yamamoto, Y. Polariton lasing vs. photon lasing in a semiconductor microcavity. *Proc. Natl Acad. Sci. USA* **100**, 15318–15323 (2003).
7. Ebbesen, T. W. Hybrid light–matter states in a molecular and material science perspective. *Acc. Chem. Res.* **49**, 2403–2412 (2016).
8. Ghosh, S. & Liew, T. C. H. Quantum computing with exciton-polariton condensates. *npj Quantum Inf.* **6**, 16 (2020).
9. Chernikov, A. et al. Exciton binding energy and nonhydrogenic Rydberg series in monolayer WS2. *Phys. Rev. Lett.* **113**, 076802 (2014).
10. Wang, Q. H., Kalantar-Zadeh, K., Kis, A., Coleman, J. N. & Strano, M. S. Electronics and optoelectronics of two-dimensional transition metal dichalcogenides. *Nat. Nanotechnol.* **7**, 699–712 (2012).
11. Manzeli, S., Ovchinnikov, D., Pasquier, D., Yazyev, O. V. & Kis, A. 2D transition metal dichalcogenides. *Nat. Rev. Mater.* **2**, 17033 (2017).
12. Mak, K. F. & Shan, J. Photonics and optoelectronics of 2D semiconductor transition metal dichalcogenides. *Nat. Photonics* **10**, 216–226 (2016).
13. Li, Y. et al. Measurement of the optical dielectric function of monolayer transition-metal dichalcogenides: MoS2, MoSe2, WS2, and WSe2. *Phys. Rev. B* **90**, 205422 (2014).
14. Kleemann, M.-E. et al. Strong-coupling of WSe2 in ultra-compact plasmonic nanocavities at room temperature. *Nat. Commun.* **8**, 1296 (2017).
15. Liu, L. et al. Strong plasmon–exciton interactions on nanoantenna array–monolayer WS2 hybrid system. *Adv. Opt. Mater.* **8**, 1901002 (2020).
16. Tang, Y. et al. Ultrafast response of a hybrid device based on strongly coupled monolayer WS2 and photonic crystals: the effect of photoinduced coulombic screening. *Laser Photonics Rev.* **14**, 1900419 (2020).
17. Kravtsov, V. et al. Nonlinear polaritons in a monolayer semiconductor coupled to optical bound states in the continuum. *Light Sci. Appl.* **9**, 56 (2020).
18. Dufferwiel, S. et al. Exciton–polaritons in van der Waals heterostructures embedded in tunable microcavities. *Nat. Commun.* **6**, 8579 (2015).
19. Munkhbat, B. et al. Self-hybridized exciton-polaritons in multilayers of transition metal dichalcogenides for efficient light absorption. *ACS Photonics* **6**, 139–147 (2019).
20. Verre, R. et al. Transition metal dichalcogenide nanodisks as high-index dielectric Mie nanoresonators. *Nat. Nanotechnol.* **14**, 679–683 (2019).
21. Wang, J. et al. All-dielectric crescent metasurface sensor driven by bound states in the continuum. *Adv. Funct. Mater.* **31**, 2104652 (2021).
22. Tittl, A. et al. Imaging-based molecular barcoding with pixelated dielectric metasurfaces. *Science* **360**, 1105–1109 (2018).
23. Gao, X., Zhen, B., Soljačić, M., Chen, H. & Hsu, C. W. Bound states in the continuum in Fiber Bragg gratings. *ACS Photonics* **6**, 2996–3002 (2019).
24. Zograf, G. et al. High-harmonic generation from resonant dielectric metasurfaces empowered by bound states in the continuum. *ACS Photonics* **9**, 567–574 (2022).
25. Yang, J. et al. Low-threshold bound state in the continuum lasers in hybrid lattice resonance metasurfaces. *Laser Photonics Rev.* **15**, 2100118 (2021).
26. Koshelev, K., Lepeshov, S., Liu, M., Bogdanov, A. & Kivshar, Y. Asymmetric metasurfaces with high-Q resonances governed by bound states in the continuum. *Phys. Rev. Lett.* **121**, 193903 (2018).
27. Kühne, J. et al. Fabrication robustness in BIC metasurfaces. *Nanophotonics* **10**, 4305–4312 (2021).
28. Xie, P. et al. Strong coupling between excitons in a two-dimensional atomic crystal and quasibound states in the continuum in a two-dimensional all-dielectric asymmetric metasurface. *Phys. Rev. B* **104**, 125446 (2021).
29. Koshelev, K. L., Sychev, S. K., Sadrieva, Z. F., Bogdanov, A. A. & Iorsh, I. V. Strong coupling between excitons in transition metal dichalcogenides and optical bound states in the continuum. *Phys. Rev. B* **98**, 161113 (2018).
30. Cao, S. et al. Normal-incidence-excited strong coupling between excitons and symmetry-protected quasi-bound states in the continuum in silicon nitride–WS2 heterostructures at room temperature. *J. Phys. Chem. Lett.* **11**, 4631–4638 (2020).
31. Zhang, X. & Bradley, A. L. Polaritonic critical coupling in a hybrid quasibound states in the continuum cavity–WS2 monolayer system. *Phys. Rev. B* **105**, 165424 (2022).
32. Sortino, L. et al. Enhanced light-matter interaction in an atomically thin semiconductor coupled with dielectric nano-antennas. *Nat. Commun.* **10**, 5119 (2019).
33. Kühner, L. et al. Radial bound states in the continuum for polarization-invariant nanophotonics. *Nat. Commun.* **13**, 4992 (2022).
34. Zhang, H. et al. Hybrid exciton-plasmon-polaritons in van der Waals semiconductor gratings. *Nat. Commun.* **11**, 3552 (2020).
35. Bernhardt, N. et al. Quasi-BIC resonant enhancement of second-harmonic generation in WS2 monolayers. *Nano Lett.* **20**, 5309–5314 (2020).
36. Adato, R., Artar, A., Erramilli, S. & Altug, H. Engineered absorption enhancement and induced transparency in coupled molecular and plasmonic resonator systems. *Nano Lett.* **13**, 2584–2591 (2013).
37. Zhang, L., Gogna, R., Burg, W., Tutuc, E. & Deng, H. Photonic-crystal exciton-polaritons in monolayer semiconductors. *Nat. Commun.* **9**, 713 (2018).
38. Molas, M. R. et al. The optical response of monolayer, few-layer and bulk tungsten disulfide. *Nanoscale* **9**, 13128–13141 (2017).
39. Al-Ani, I. A. M. et al. Strong coupling of exciton and high-Q mode in all-perovskite metasurfaces. *Adv. Opt. Mater.* **10**, 2101120 (2022).
40. Al-Ani, I. A. M., As'Ham, K., Huang, L., Miroshnichenko, A. E. & Hattori, H. T. Enhanced strong coupling of TMDC monolayers by bound state in the continuum. *Laser Photonics Rev.* **15**, 2100240 (2021).
41. Dovzhenko, D. S., Ryabchuk, S. V., Rakovich, Yu. P. & Nabiev, I. R. Light–matter interaction in the strong coupling regime: configurations, conditions, and applications. *Nanoscale* **10**, 3589–3605 (2018).
42. Tserkezis, C. et al. On the applicability of quantum-optical concepts in strong-coupling nanophotonics. *Rep. Prog. Phys.* **83**, 082401 (2020).
43. Shen, F. et al. Transition metal dichalcogenide metaphotonic and self-coupled polaritonic platform grown by chemical vapor deposition. *Nat. Commun.* **13**, 5597 (2022).

Methods

Numerical simulation

Simulations were conducted with CST Studio Suite 2021 using periodic Floquet boundary conditions and a plane-wave excitation polarized along the long axis of the rods with normal incidence angle. The WS_2 material data used throughout the paper were adapted from tabulated permittivity data for monolayer WS_2 from ref. 44 by fitting a Tauc–Lorentz model with four oscillators to represent the in-plane permittivity. We accounted for the spectral shift of the exciton and a reduction of oscillator strength for the bulk material by changing the corresponding values of the material and confirmed the correctness of simulation by comparing with results from optical characterization. This method allows a combination of a multitude of non-radiative loss channels, such as material absorption, surface scattering and the effect of nanostructuring on the exciton into an empirical permittivity model, yielding excellent experimental agreement while reducing computational complexity. The exact formulas and parameters can be found in Supporting Note 1. The out-of-plane permittivity was set to $\varepsilon = 7 + 0i$.

Nanofabrication

WS_2 flakes were transferred from bulk crystals (HQ Graphene) onto fused silica substrates via mechanical exfoliation. By controlling exfoliation parameters, such as the heat treatment temperature, exfoliation time and applied pressure, we optimized the yield of the flakes with thicknesses ranging from 30 to 50 nm to achieve an adequate area to host a multitude of BIC metasurfaces. The metasurface patches have a footprint of $35 \times 35\ \mu m^2$, which ensures a sufficient number of more than 50×50 unit cells for each scaling factor—a necessity to excite the collective BIC resonance with stable Q factor[45]. The substrates were treated with oxygen plasma to enhance the adhesion and the deposition took place at elevated temperatures of above 100 °C to remove moisture and to stretch out the tape used for exfoliation, which subsequently flattened the TMDC flakes to avoid shattering into small shards. Small mechanical pressure was applied during deposition. For alignment purposes, a marker system was fabricated onto the substrates via optical lithography (SÜSS Maskaligner MA6) before exfoliation. The height of the flakes was measured with a profilometer (Bruker Dektak XT) using a stylus with a radius of 2 µm, providing sub-nanometre resolution. A layer of PMMA 950k resist followed by Espacer 300Z was spin-coated onto the sample, after which the metasurface design was written into the resist via EBL (Raith ELine Plus). A gold hardmask was deposited with e-beam evaporation followed by a lift-off in Microposit Remover 1165. Finally, the design was etched into the flakes using RIE (Oxford PlasmaPro 100) with a SF_6-based chemistry at a pressure of 20 mTorr and a radio frequency (RF) power of 50 W. The hardmask was removed in a solution of potassium monoiodide and iodine (Sigma-Aldrich).

Optical characterization

The samples were characterized in a confocal optical transmission microscope with from-the-bottom illumination with collimated and linear polarized white light. The light was collected using a ×50 objective with a numerical aperture of 0.8, dispersed in a spectrometer with a grating groove density of 150 mm^{-1} and detected with a SI-CCD sensor.

The low-temperature transmittance measurements were performed in a variable-temperature helium flow cryostat with a confocal microscope in transmission configuration. Thermal light from a tungsten halogen light source was used for excitation and was focused from-the-bottom into the sample. The light transmitted through the sample was collected using a ×20 objective with a numerical aperture of 0.4. A pinhole was used as a spatial filter in the detection path yielding a detection spot size of around 7 µm. The large footprints of the metasurfaces were leveraged to collect light only in the centre of the arrays, which mitigates edge effects and allows for optimal signal modulations. The collected light was analysed in a 500 mm spectrometer using a 150 grooves per mm grating and detected using a CCD sensor.

Reporting summary

Further information on research design is available in the Nature Portfolio Reporting Summary linked to this article.

Data availability

The main data supporting the findings of this study are available within the article and its Supplementary Information files. Extra data are available from the corresponding author upon reasonable request.

References

44. Jung, G.-H., Yoo, S. & Park, Q.-H. Measuring the optical permittivity of two-dimensional materials without a priori knowledge of electronic transitions. *Nanophotonics* **8**, 263–270 (2018).
45. Liu, Z. et al. High-Q quasibound states in the continuum for nonlinear metasurfaces. *Phys. Rev. Lett.* **123**, 253901 (2019).

Acknowledgements

We thank K. Koshelev and Y. Kivshar for helpful discussions. This work was supported by the Deutsche Forschungsgemeinschaft (DFG, German Research Foundation) under Germany's Excellence Strategy (EXC 2089/1—390776260 and EXC-2111—390814868), the Emmy Noether Programme (TI 1063/1), the Bavarian programme Solar Energies Go Hybrid (SolTech), the Center for NanoScience (CeNS), the Alexander von Humboldt Foundation (Humboldt Research Fellowship to L.S.), the International Max Planck Research School for Quantum Science and Technology (IMPRS-QST) (funding to A.B.M.), the EPSRC (EP/W017075/1 to S.A.M.) and the Lee-Lucas Chair in Physics (to S.A.M.).

Author contributions

T.W., L.K. and A.T. conceived the idea and planned the research. T.W., L.K. and J.K. contributed to the sample fabrication. T.W. performed optical measurements at room temperature. T.W., A.B.M. and N.P.W. performed optical measurements in the cryostat. T.W. conducted the numerical simulations and data processing. T.W., A.T., L.K. and L.S. contributed to the data analysis. J.J.F., S.A.M. and A.T. supervised the project. All authors contributed to the writing of the paper.

Competing interests

The authors declare no competing interests.

Additional information

Supplementary information The online version contains supplementary material available at https://doi.org/10.1038/s41563-023-01580-7.

Correspondence and requests for materials should be addressed to Andreas Tittl.

Peer review information *Nature Materials* thanks Andrey Bogdanov, Artur Davoyan and the other, anonymous, reviewer(s) for their contribution to the peer review of this work.

nature portfolio

Corresponding author(s): Andreas Tittl

Last updated by author(s): May 2, 2023

Reporting Summary

Nature Portfolio wishes to improve the reproducibility of the work that we publish. This form provides structure for consistency and transparency in reporting. For further information on Nature Portfolio policies, see our Editorial Policies and the Editorial Policy Checklist.

Statistics

For all statistical analyses, confirm that the following items are present in the figure legend, table legend, main text, or Methods section.

n/a	Confirmed	
☒	☐	The exact sample size (*n*) for each experimental group/condition, given as a discrete number and unit of measurement
☒	☐	A statement on whether measurements were taken from distinct samples or whether the same sample was measured repeatedly
☒	☐	The statistical test(s) used AND whether they are one- or two-sided *Only common tests should be described solely by name; describe more complex techniques in the Methods section.*
☒	☐	A description of all covariates tested
☒	☐	A description of any assumptions or corrections, such as tests of normality and adjustment for multiple comparisons
☒	☐	A full description of the statistical parameters including central tendency (e.g. means) or other basic estimates (e.g. regression coefficient) AND variation (e.g. standard deviation) or associated estimates of uncertainty (e.g. confidence intervals)
☒	☐	For null hypothesis testing, the test statistic (e.g. *F*, *t*, *r*) with confidence intervals, effect sizes, degrees of freedom and *P* value noted *Give P values as exact values whenever suitable.*
☒	☐	For Bayesian analysis, information on the choice of priors and Markov chain Monte Carlo settings
☒	☐	For hierarchical and complex designs, identification of the appropriate level for tests and full reporting of outcomes
☒	☐	Estimates of effect sizes (e.g. Cohen's *d*, Pearson's *r*), indicating how they were calculated

Our web collection on statistics for biologists contains articles on many of the points above.

Software and code

Policy information about availability of computer code

Data collection	*Provide a description of all commercial, open source and custom code used to collect the data in this study, specifying the version used OR state that no software was used.*
Data analysis	*Provide a description of all commercial, open source and custom code used to analyse the data in this study, specifying the version used OR state that no software was used.*

For manuscripts utilizing custom algorithms or software that are central to the research but not yet described in published literature, software must be made available to editors and reviewers. We strongly encourage code deposition in a community repository (e.g. GitHub). See the Nature Portfolio guidelines for submitting code & software for further information.

Data

Policy information about availability of data

All manuscripts must include a data availability statement. This statement should provide the following information, where applicable:

- Accession codes, unique identifiers, or web links for publicly available datasets
- A description of any restrictions on data availability
- For clinical datasets or third party data, please ensure that the statement adheres to our policy

The main data supporting the findings of this study are available within the article and its Supplementary Information files. Extra data are available from the corresponding author upon reasonable request.

Human research participants

Policy information about studies involving human research participants and Sex and Gender in Research.

Reporting on sex and gender	*Use the terms sex (biological attribute) and gender (shaped by social and cultural circumstances) carefully in order to avoid confusing both terms. Indicate if findings apply to only one sex or gender; describe whether sex and gender were considered in study design whether sex and/or gender was determined based on self-reporting or assigned and methods used. Provide in the source data disaggregated sex and gender data where this information has been collected, and consent has been obtained for sharing of individual-level data; provide overall numbers in this Reporting Summary. Please state if this information has not been collected. Report sex- and gender-based analyses where performed, justify reasons for lack of sex- and gender-based analysis.*
Population characteristics	*Describe the covariate-relevant population characteristics of the human research participants (e.g. age, genotypic information, past and current diagnosis and treatment categories). If you filled out the behavioural & social sciences study design questions and have nothing to add here, write "See above."*
Recruitment	*Describe how participants were recruited. Outline any potential self-selection bias or other biases that may be present and how these are likely to impact results.*
Ethics oversight	*Identify the organization(s) that approved the study protocol.*

Note that full information on the approval of the study protocol must also be provided in the manuscript.

Field-specific reporting

Please select the one below that is the best fit for your research. If you are not sure, read the appropriate sections before making your selection.

☐ Life sciences ☐ Behavioural & social sciences ☐ Ecological, evolutionary & environmental sciences

For a reference copy of the document with all sections, see nature.com/documents/nr-reporting-summary-flat.pdf

Life sciences study design

All studies must disclose on these points even when the disclosure is negative.

Sample size	*Describe how sample size was determined, detailing any statistical methods used to predetermine sample size OR if no sample-size calculation was performed, describe how sample sizes were chosen and provide a rationale for why these sample sizes are sufficient.*
Data exclusions	*Describe any data exclusions. If no data were excluded from the analyses, state so OR if data were excluded, describe the exclusions and the rationale behind them, indicating whether exclusion criteria were pre-established.*
Replication	*Describe the measures taken to verify the reproducibility of the experimental findings. If all attempts at replication were successful, confirm this OR if there are any findings that were not replicated or cannot be reproduced, note this and describe why.*
Randomization	*Describe how samples/organisms/participants were allocated into experimental groups. If allocation was not random, describe how covariates were controlled OR if this is not relevant to your study, explain why.*
Blinding	*Describe whether the investigators were blinded to group allocation during data collection and/or analysis. If blinding was not possible, describe why OR explain why blinding was not relevant to your study.*

Behavioural & social sciences study design

All studies must disclose on these points even when the disclosure is negative.

Study description	*Briefly describe the study type including whether data are quantitative, qualitative, or mixed-methods (e.g. qualitative cross-sectional, quantitative experimental, mixed-methods case study).*
Research sample	*State the research sample (e.g. Harvard university undergraduates, villagers in rural India) and provide relevant demographic information (e.g. age, sex) and indicate whether the sample is representative. Provide a rationale for the study sample chosen. For studies involving existing datasets, please describe the dataset and source.*
Sampling strategy	*Describe the sampling procedure (e.g. random, snowball, stratified, convenience). Describe the statistical methods that were used to predetermine sample size OR if no sample-size calculation was performed, describe how sample sizes were chosen and provide a rationale for why these sample sizes are sufficient. For qualitative data, please indicate whether data saturation was considered, and what criteria were used to decide that no further sampling was needed.*

Data collection	*Provide details about the data collection procedure, including the instruments or devices used to record the data (e.g. pen and paper, computer, eye tracker, video or audio equipment) whether anyone was present besides the participant(s) and the researcher, and whether the researcher was blind to experimental condition and/or the study hypothesis during data collection.*
Timing	*Indicate the start and stop dates of data collection. If there is a gap between collection periods, state the dates for each sample cohort.*
Data exclusions	*If no data were excluded from the analyses, state so OR if data were excluded, provide the exact number of exclusions and the rationale behind them, indicating whether exclusion criteria were pre-established.*
Non-participation	*State how many participants dropped out/declined participation and the reason(s) given OR provide response rate OR state that no participants dropped out/declined participation.*
Randomization	*If participants were not allocated into experimental groups, state so OR describe how participants were allocated to groups, and if allocation was not random, describe how covariates were controlled.*

Ecological, evolutionary & environmental sciences study design

All studies must disclose on these points even when the disclosure is negative.

Study description	*Briefly describe the study. For quantitative data include treatment factors and interactions, design structure (e.g. factorial, nested, hierarchical), nature and number of experimental units and replicates.*
Research sample	*Describe the research sample (e.g. a group of tagged Passer domesticus, all Stenocereus thurberi within Organ Pipe Cactus National Monument), and provide a rationale for the sample choice. When relevant, describe the organism taxa, source, sex, age range and any manipulations. State what population the sample is meant to represent when applicable. For studies involving existing datasets, describe the data and its source.*
Sampling strategy	*Note the sampling procedure. Describe the statistical methods that were used to predetermine sample size OR if no sample-size calculation was performed, describe how sample sizes were chosen and provide a rationale for why these sample sizes are sufficient.*
Data collection	*Describe the data collection procedure, including who recorded the data and how.*
Timing and spatial scale	*Indicate the start and stop dates of data collection, noting the frequency and periodicity of sampling and providing a rationale for these choices. If there is a gap between collection periods, state the dates for each sample cohort. Specify the spatial scale from which the data are taken*
Data exclusions	*If no data were excluded from the analyses, state so OR if data were excluded, describe the exclusions and the rationale behind them, indicating whether exclusion criteria were pre-established.*
Reproducibility	*Describe the measures taken to verify the reproducibility of experimental findings. For each experiment, note whether any attempts to repeat the experiment failed OR state that all attempts to repeat the experiment were successful.*
Randomization	*Describe how samples/organisms/participants were allocated into groups. If allocation was not random, describe how covariates were controlled. If this is not relevant to your study, explain why.*
Blinding	*Describe the extent of blinding used during data acquisition and analysis. If blinding was not possible, describe why OR explain why blinding was not relevant to your study.*

Did the study involve field work? ☐ Yes ☐ No

Field work, collection and transport

Field conditions	*Describe the study conditions for field work, providing relevant parameters (e.g. temperature, rainfall).*
Location	*State the location of the sampling or experiment, providing relevant parameters (e.g. latitude and longitude, elevation, water depth).*
Access & import/export	*Describe the efforts you have made to access habitats and to collect and import/export your samples in a responsible manner and in compliance with local, national and international laws, noting any permits that were obtained (give the name of the issuing authority, the date of issue, and any identifying information).*
Disturbance	*Describe any disturbance caused by the study and how it was minimized.*

Reporting for specific materials, systems and methods

We require information from authors about some types of materials, experimental systems and methods used in many studies. Here, indicate whether each material, system or method listed is relevant to your study. If you are not sure if a list item applies to your research, read the appropriate section before selecting a response.

Materials & experimental systems

n/a	Involved in the study
☒	☐ Antibodies
☒	☐ Eukaryotic cell lines
☒	☐ Palaeontology and archaeology
☒	☐ Animals and other organisms
☒	☐ Clinical data
☒	☐ Dual use research of concern

Methods

n/a	Involved in the study
☒	☐ ChIP-seq
☒	☐ Flow cytometry
☒	☐ MRI-based neuroimaging